ADVANCED HEALTHCARE MATERIALS
www.advhealthmat.de

Smart Design of ZnFe and ZnFe@Fe Nanoparticles for MRI-Tracked Magnetic Hyperthermia Therapy: Challenging Classical Theories of Nanoparticles Growth and Nanomagnetism

Carlos Caro, Cinzia Guzzi, Irene Moral-Sánchez, Jesús David Urbano-Gámez, Ana M. Beltrán, and Maria Luisa García-Martín**

Iron Oxide Nanoparticles (IONPs) hold the potential to exert significant influence on fighting cancer through their theranostics capabilities as contrast agents (CAs) for magnetic resonance imaging (MRI) and as mediators for magnetic hyperthermia (MH). In addition, these capabilities can be improved by doping IONPs with other elements. In this work, the synthesis and characterization of single-core and alloy ZnFe novel magnetic nanoparticles (MNPs), with improved magnetic properties and more efficient magnetic-to-heat conversion, are reported. Remarkably, the results challenge classical nucleation and growth theories, which cannot fully predict the final size/shape of these nanoparticles and, consequently, their magnetic properties, implying the need for further studies to better understand the nanomagnetism phenomenon. On the other hand, leveraging the enhanced properties of these new NPs, successful tumor therapy by MH is achieved following their intravenous administration and tumor accumulation via the enhanced permeability and retention (EPR) effect. Notably, these results are obtained using a single low dose of MNPs and a single exposure to clinically suitable alternating magnetic fields (AMF). Therefore, as far as the authors are aware, for the first time, the successful application of intravenously administered MNPs for MRI-tracked MH tumor therapy in passively targeted tumor xenografts using clinically suitable conditions is demonstrated.

1. Introduction

Magnetic nanoparticles (MNPs) have long been applied in various biomedical applications, including bioimaging, drug delivery, and magnetic hyperthermia.[1–3] In particular, iron oxide (magnetite (Fe_3O_4) and maghemite (γ-Fe_2O_3)) NPs (IONPs) have attracted a great deal of attention among researchers due to, and not only, their exquisite magnetic properties and low toxicity.[4–6] Magnetization (magnetic moment per unit volume) can be defined as the measurement of the density of a permanent or an induced dipole moment in any magnetic field.[7] IONPs with large crystallite sizes have dipoles arranged in multiple domains in order to maintain the lowest energy state, whereas below a critical size (usually below 100 nm), the energetically unfavorable state results in single-domain IONPs. Single-domain IONPs no longer exhibit hysteresis behavior under an external magnetic field, which is known as superparamagnetism.[8,9] Moreover, doped-IONPs can improve

C. Caro, C. Guzzi, I. Moral-Sánchez, J. D. Urbano-Gámez, M. L. García-Martín
Biomedical Magnetic Resonance Laboratory-BMRL
Andalusian Public Foundation Progress and Health-FPS
Seville 41092, Spain
E-mail: ccaro@ibima.eu; mlgarcia@ibima.eu

The ORCID identification number(s) for the author(s) of this article can be found under https://doi.org/10.1002/adhm.202304044

DOI: 10.1002/adhm.202304044

C. Caro, C. Guzzi, I. Moral-Sánchez, J. D. Urbano-Gámez, M. L. García-Martín
Instituto de Investigación Biomédica de Málaga y Plataforma en Nanomedicina (IBIMA Plataforma BIONAND)
Universidad de Málaga
C/Severo Ochoa, 35, Malaga 29590, Spain

A. M. Beltrán
Departamento de Ingeniería y Ciencia de los Materiales y del Transporte
Escuela Politécnica Superior
Universidad de Sevilla
Virgen de África 7, Sevilla 41011, Spain

M. L. García-Martín
Biomedical Research Networking Center in Bioengineering
Biomaterials & Nanomedicine (CIBER-BBN)
Madrid 28029, Spain

the magnetic properties of the single-component counterpart due to increments in the magnetic permeability or electrical resistivity.[10–12] Furthermore, the magnetic properties of single-core IONPs can be improved through the production of bi-magnetic core–shell-like structures because of exchange anisotropy at the interface between their magnetic phases (exchange-coupling phenomenon).[13–15] Thus, due to their remarkable properties, IONPs have the potential to drastically impact a wide variety of biomedical applications. In particular, IONPs can be used as contrast agents (CAs) for magnetic resonance imagining (MRI),[16–19] as drug delivery nanocarriers,[20,21] or as magnetic hyperthermia (MH) mediators for cancer therapy.[22–24]

Cancer continues to be one of the main causes of death worldwide, with almost 10.0 million cancer deaths in 2020.[25] In this scenario, medical imaging is undoubtedly the most valuable tool for fighting cancer through early diagnosis,[26] with MRI playing a prominent role in monitoring structural, functional, and molecular changes in cancer tissue.[27] Additionally, the diagnostic accuracy of MRI can be improved by using CAs.[28] However, gadolinium-based CAs, which are by far the most widely used in clinical diagnosis, present some limitations related to toxic effects,[29] which has led to extensive research on the development of new CAs, IONPs being one of the most promising alternatives. Regarding the therapeutic approach of cancer, the standard strategy for malignant tumors usually involves resection of the tumor tissue, followed by localized radiotherapy and/or systemic chemotherapy,[30] with the consequent limitations related to the numerous and undesirable side effects.[31] Thus, new nanotechnology-based therapeutic approaches are emerging as promising options to tackle cancer. An example of these new strategies is the one developed by NanoTherm (MagForce AG, Berlin, Germany), which constitutes the only nanoformulation approved by the European Medicines Agency (EMA) and by the Food and Drug Administration (FDA) for the stereotactic intratumoral treatment of some particular tumors by magnetic hyperthermia using alternative magnetic fields (AMF) with a frequency of 100 kHz and a magnetic field amplitude in the range 12–18 kA m^{-1} (≈16–23 mT).[32–34] However, NanoTherm tends to aggregate, hampering its intravenous administration,[35] which is typically the preferred administration route to achieve a more homogeneous tumor targeting and specifically to target the well-vascularized and, therefore, more active regions of the tumor, thus enhancing treatment effectiveness. In fact, the development of NPs for tumor theranostic has relied on the well-known Enhanced Permeability and Retention (EPR) effect, which has been considered the most efficient mechanism for accumulating NPs with hydrodynamic diameters (HD) between 20 and 100 nm.[36–38] However, there is currently a great deal of controversy questioning the suitability of the EPR effect as an efficient mechanism for the delivery of NPs to tumors at intratumoral therapeutic doses.[39,40] In the case of MH, the therapeutic dose not only depends on the amount of NPs but also on their capacity as MH mediators, that is, their Specific Absorption Rate (SAR). Therefore, combining optimized stealth properties and prolonged circulation times to improve the EPR effect, together with a higher SAR, may allow for efficient MH tumor therapy following the intravenous administration of MNPs.

To this end, we synthesized single-core and alloy ZnFe NPs by thermal decomposition and performed a comprehensive characterization aiming to shed some light on classical growth theories and thus aid their smart design. Moreover, classical nanomagnetism theories were investigated in depth to assess their capacity to explain the performance of our NPs as CAs and their magnetic-to-heat conversion features. Then, after cytotoxicity evaluation of all NPs, ZnFe NP was selected as the most suitable one for in vivo studies. After intravenous injection of these NPs in breast tumor-bearing mice, ZnFe NPs were tracked in vivo by MRI, showing an appreciable tumor accumulation through the EPR effect after 24 h, which was sufficient for a successful MH therapeutic response with a single dose and a single exposure to 121.85 kHz AMF.

2. Experimental Section

2.1. Materials

Iron (III) chloride, zinc (II) chloride, sodium oleate, oleic acid 99%, gallic acid, polyethylene glycol (PEG) 3000 Da, 1-octadecene, triethylamine, 4-Dimethylaminopyridine, dicyclohexyl carbodiimide (DCC), 3-[4,5-dimethylthiazol-2yl]-2,5-diphenyl tetrazolium bromide (MTT), 4′,6-diamidino-2-phenylindole (DAPI), phosphate-buffered saline (PBS) and ethanol 99% were obtained from Sigma Aldrich. TO-PRO-3 Iodide was purchased from Thermofisher. Dimethyl sulfoxide (DMSO), toluene, acetone, hexane, chloroform, dichloromethane, and tetrahydrofuran were supplied by Acros Organics. Dulbecco's Modified Eagle Medium (DMEM), Roswell Park Memorial Institute (RPMI), Fetal Bovine Serum (FBS), L-glutamine, and penicillin/streptomycin solution were obtained from Gibco. All reagents were used as received without further purification. Milli-Q water (18.2 MΩ, filtered with filter pore size 0.22 µm) from Millipore.

2.2. Synthesis of the Single-Core and Core–Shell/Alloy Nanoparticles

2.2.1. Synthesis of Metal Oleates

Metal precursors were synthesized following a previously mentioned protocol with modifications.[41] Further details are described in the Supporting Information.

2.2.2. Synthesis of ZnFe1

Briefly, 2 g of Iron-Zinc Oleate (ratio 4:1) and 0.3 g of oleic acid were solved under vigorous stirring in 15 mL of 1-octadecene. Then, the temperature was increased till 30 °C, followed by 3 cycles of vacuum/N_2 (10 min). At this point, the reaction was heated to 320 °C by applying a constant heating rate of 3 °C min^{-1}, under nitrogen. These conditions were maintained for 1 h, followed by the cooling down to room temperature. Finally, the NPs were washed 3 times with ethanol/acetone (ratio 1/1) and resuspended in toluene.

2.2.3. Synthesis of ZnFe2

1.6 g of Iron oleate, 0.4 g of Zinc oleate, and 0.3 g of oleic acid were solved under vigorous stirring in 15 mL of 1-octadecene. From this point, the protocol was the same as described for ZnFe1.

2.2.4. Synthesis of ZnFe3

These nanoparticles were synthesized similarly as described for ZnFe1, but the metal precursor was changed to Iron-Zinc Oleate (ratio 2:1).

2.2.5. Synthesis of ZnFeX@Fe

Either ZnFe1 or ZnFe2 NPs were mixed with iron oleate (iron ratio 1:1 molar) and 0.28 g of oleic acid. Then, these chemicals were dissolved in 15 mL of 1-octadecene under stirring. At this point, 3 cycles of 20 min (vacuum/N_2) were applied to the mixture. The reaction was heated for 1 h at 320 °C, under nitrogen and applying a constant heating rate of 3 °C min^{-1}, followed by a cooling down step till room temperature. Finally, NPs were washed as previously described for ZnFeX NPs.

2.3. Functionalization of Magnetic Nanoparticles

The synthesis of the PEGylated ligand and the subsequent ligand exchange process were conducted as described previously by some of the authors.[42,43] Detailed protocols are described in the Supporting Information.

2.4. Characterization Methods

Nanoparticles were thoroughly characterized by Transmission Electron Microscopy (TEM), High Angle Annular Dark Field Scanning-Transmission Electron Microscopy (HAADF -STEM), X-ray diffraction (XRD), Inductively Coupled Plasma High-Resolution Mass Spectroscopy (ICP-HRMS), Fourier Transform Infra-Red Spectroscopy (FTIR), Dynamic Light Scattering (DLS), Vibrating-sample magnetometer (VSM), Specific Absorption Rate (SAR) measurement and relaxivity measurements. The complete protocols are described in detail in the Supporting Information.

2.5. Cell Toxicity Assessment

2.5.1. Cell Culture

Two different cells were selected as working models. HFF-1 human fibroblast cells were selected as control cells to evaluate the potential side effects, using DMEM as the growth medium (supplemented with L-glutamine (2 mM), FBS (10%), and penicillin/streptomycin (1%)), whereas 4T1 mice stage IV breast cancer cells were selected for cell uptake and in vivo model of cancer, using RPMI as growth medium (supplemented with L-glutamine (2 mM), FBS (10%) and penicillin/streptomycin (1%)). Both cell lines were cultured at 37 °C in an incubator (5% CO_2).

2.5.2. Cytotoxicity Assays

Cytotoxicity of nanoparticles was evaluated in HFF-1 cells by optical microscopy, life-dead assay, and MTT assay. Different aspects related to cell viability (cell morphology, total number of cells, number of necrotic/late apoptotic cells, intracellular esterase activity, and mitochondrial activity) were evaluated.

2.6. In Vivo Studies

2.6.1. Mice Experiments

Female Balb/c mice (20 g in weight) provided by Charles River (n = 4 per experimental group) were used for in vivo experiments. In vivo experiments were conducted in accordance with the Spanish and European Guidelines for Care and Use of Laboratory Animals (R.D. 53/2013 and 2010/62/UE) and approved by the local ethical committee and the Highest Institutional Ethical Committee (Andalusian Government, accreditation number 14/09/2021/129). ZnFe NPs were intravenously injected in a concentration of 10 mg Fe kg^{-1}. This concentration was chosen based on previous studies conducted by the group that demonstrated the safety of this dose, without any appreciable toxic effect, while providing high MRI contrast. Yet, higher doses may be used in future MH studies if deemed necessary and safe.

2.6.2. In Vivo Magnetic Resonance Imaging (MRI)

MRI experiments were conducted on the 9.4 T Bruker Biospec system, using protocols described by some of the authors elsewhere[44] and in the Supporting Information.

2.6.3. Tumor Implantation

4T1 orthotopic breast tumors were selected as a murine cancer model. Cells were brought to 80–90% confluence in culture. Then, mice were anesthetized with isoflurane 1%, and cells were injected orthotopically (1×10^6 cells) in the right mammary fat pad.

2.6.4. In Vivo Treatment

When tumors reached 0.25 cm^3, mice were divided randomly into 2 groups, named G1 (NaCl intravenously injected + AMF exposure (MH)) and G2 (NPs intravenously injected + MH). NPs were injected via the tail vein. At 24 h, mice were placed in a DM5 Nanoscale Biomagnetic instrument and exposed to an AMF (Frequency (f) = 121.85 kHz, Magnetic Field Amplitude (H) = 220 Gauss or 17.5 kA m^{-1}) for 30 min.

2.6.5. Histology

Animals were sacrificed at the endpoint of the experiments, and samples from various tissues were collected. Tissue samples

were then processed and stained with Hematoxylin and Eosin (H&E), and Prussian Blue prior to histological evaluation by light microscopy. Hematoxylin and Eosin (H&E) staining was used to assess tissue architecture, and Prussian blue staining to assess colloidal iron deposits. Protocols are described in detail in the Supporting Information.

2.7. Statistical Analysis

The statistical analysis was performed using the Jamovi software 2.3.21. Mann–Whitney *U* test was selected for cell viability and in vivo T_2 analysis, whereas, for the in vivo follow-up of the treatment, Welch's *t*-test was selected ($p < 0.05$). Values are shown as mean ± standard deviation (SD).

3. Results and Discussion

3.1. Nanoparticles Characterization

As mentioned previously, core–shell-like structures can improve the magnetic properties of the single-core counterpart. Thus, in this work, three single-core (ZnFe1, ZnFe2, and ZnFe3) and two core–shell/alloy (ZnFe1@Fe and ZnFe2@Fe) magnetic NPs were synthesized and compared. The process of NPs formation can be described as the mechanism whereby metallic nuclei (seeds) act as templates for crystal growth. This mechanism is frequently described using the classical LaMer theory, which can be considered a seed-mediated growth with three stages: I) supersaturation of monomer but without the presence of NPs; II) supersaturation limit exceeds, and nucleation starts; and III) growth of NPs without further nucleation, since monomer concentration is under supersaturation limit.[45–48] The as-synthesized single-core magnetic NPs presented different sizes (ZnFe1 ≈ 32.8 nm, ZnFe2 ≈ 19.2 nm, and ZnFe3 = Heterogeneous) (**Figure 1**a,b and Figure S1a, Supporting Information), evidencing that the metallic precursor strongly determines the final size. These results are in agreement with previous reports.[49,50] ZnFe3 NPs were discarded for further experiments due to their large heterogeneity. As mentioned previously, the synthesis of NPs can be considered a seed-mediated growth process, and therefore, we used single-core NPs as seed; that is, we introduced externally the metallic nucleus in stage II of LaMer mechanism. ZnFe1 and ZnFe2 were introduced in the reaction, resulting in core–shell/alloy NPs with sizes of 20.5 and 22.8 nm for ZnFe1@Fe and ZnFe2@Fe, respectively (Figure 1a,b). Thus, ZnFe1@Fe underwent a digestive ripening (inverse of Ostwald ripening), in which larger NPs redissolve and may promote smaller particles growth.[51,52] In order to confirm the formation of a core–shell/alloy structure and the presence of Zn, two different techniques were used. On the one hand, samples were analyzed by HAADF-STEM, where intensities were proportional to $t \bullet Z^n$ (where *t* is the thickness crossed by the electron beam, Z is the atomic mass of the material, and *n* is a constant (in the range 1.6 and 1.9).[53,54] The core–shell structure could not be confirmed, and both ZnFe1@Fe and ZnFe2@Fe presented an unexpected alloy structure (Figure 1a), which might be associated with galvanic corrosion and the electrons transfer from Zn (Anode) to Fe (Cathode), in a similar manner as previously observed for other metallic NPs.[55] On the other hand, the Zn composition was confirmed by Energy-dispersive X-ray spectroscopy (EDX), showing the typical peaks associated with it, which also exhibited a relative decrease in their intensities from single-core NPs to alloy NPs (Figure 1c). Moreover, the crystalline structure of the NPs was characterized by powder XRD. The obtained pattern of ZnFe1 and ZnFe2 revealed highly intense peaks of Fe, which can be indexed to (311), (200), and (440) phases[56] (Figure 1d). Furthermore, ZnFe2@Fe exhibited a similar pattern, whereas ZnFe1@Fe displayed a broad X-ray where only (311) phase was detected, indicative of a more amorphous structure.[57,58] All the peaks observed by XRD can be attributed to either γ–Fe_2O_3 or Fe_3O_4.[59] Thus, these results indicate that, in certain cases, the introduction of NPs as seed for later growth may not lead to the formation of core–shell structures. Even more, an unexpected crystalline structure reorganization may happen, resulting in alloy NPs. Overall, none of the classical nucleation and growth theories were able to explain our results.

The as-described NPs were not stable in aqueous media due to their hydrophobic capping after the thermal decomposition process. Therefore, both single-core ZnFe NPs and alloy ZnFe@Fe NPs, were functionalized using a PEGylated ligand to render water-stable NPs, hereinafter referred to as ZnFe1-PEG, ZnFe2-PEG, ZnFe1@Fe-PEG, and ZnFe2@Fe-PEG (see Figure S3, Supporting Information). It is worth mentioning that, after the ligand exchange process, all magnetic NPs maintained shapes and sizes similar to the original ones (Figure S2, Supporting Information). Regarding the metallic composition, measured by ICP-HRMS after the ligand exchange (which should remain similar), a dramatic decay in the Zn percentage from the single-core NPs to the alloy NPs was observed (from ≈37% in the ZnFe1 and ≈42% in the ZnFe2 to ≈10% in the ZnFe1@Fe and ≈1% in the ZnFe2@Fe, respectively). These results indicate that new Fe was integrated into the alloy NPs, potentially replacing (either fully or partially) Zn. Once the ligand exchange process was conducted, the stability of the PEGylated NPs in aqueous media was validated by measuring their HD in saline (**Figure 2**a). Both single-core ZnFe NPs did not exhibit appreciable changes even after 168 h, their final HD being ≈50 and ≈60 nm for ZnFe1-PEG and ZnFe2-PEG, respectively. These HDs were in the range regarded as optimal for in vivo applications (≈50 nm).[60] On the contrary, unexpectedly poor stability was noticed for both ZnFe1@Fe-PEG and ZnFe2@Fe-PEG, suggesting that the PEGylated ligand was not able to properly interact with the NPs surface, even though alloy NPs were mainly composed of Fe.

As for the magnetic properties of NPs, it has been widely described that there is a critical diameter below which NPs behave as single-domain magnets with superparamagnetic properties. However, there is a controversy about this limit, placing it in the range of 15–30 nm.[61–63] The hysteresis loops of both ZnFe1-PEG and ZnFe2-PEG revealed a superparamagnetic behavior (Figure 2b), whereas ZnFe1@Fe-PEG exhibited unexpected paramagnetic behavior and, finally, ZnFe2@Fe-PEG showed a ferromagnetic behavior. Moreover, their specific saturation magnetizations (Ms) were 92.5, 68.2, 21.5, and 134.9 emu g^{-1}, respectively (Figure 2b). Therefore, since ZnFe1-PEG exhibited a paramagnetic behavior with a magnetic core of ≈30 nm, while ZnFe2-PEG was ferromagnetic with a magnetic core of ≈22 nm, and furthermore, both had a similar XRD and shape, it becomes evident

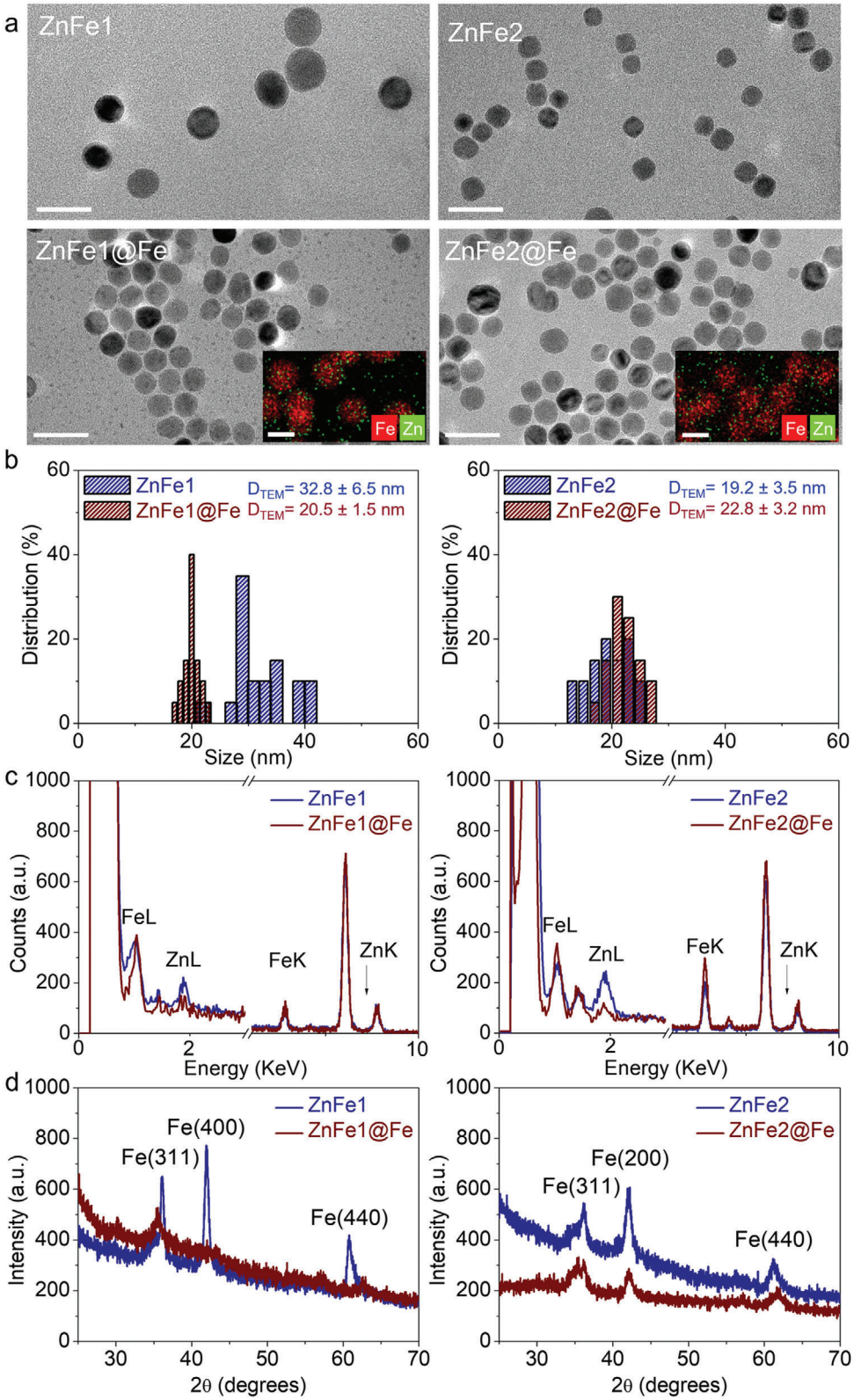

Figure 1. a) Transmission electron microscopy images of the synthesized NPs. The scale bar corresponds to 50 nm. The inset exhibits the spatial distribution of metal atoms in the NPs as measured by HAADF and EDX. The scale bar corresponds to 20 nm. b) Size distribution obtained from the counting of 100 NPs in the TEM images. c) EDX spectrum analysis showing major peaks of the NPs. d) XRD pattern of the NPs. Single-core ZnFe NPs are represented in blue, whereas alloy ZnFe@Fe NPs are represented in red.

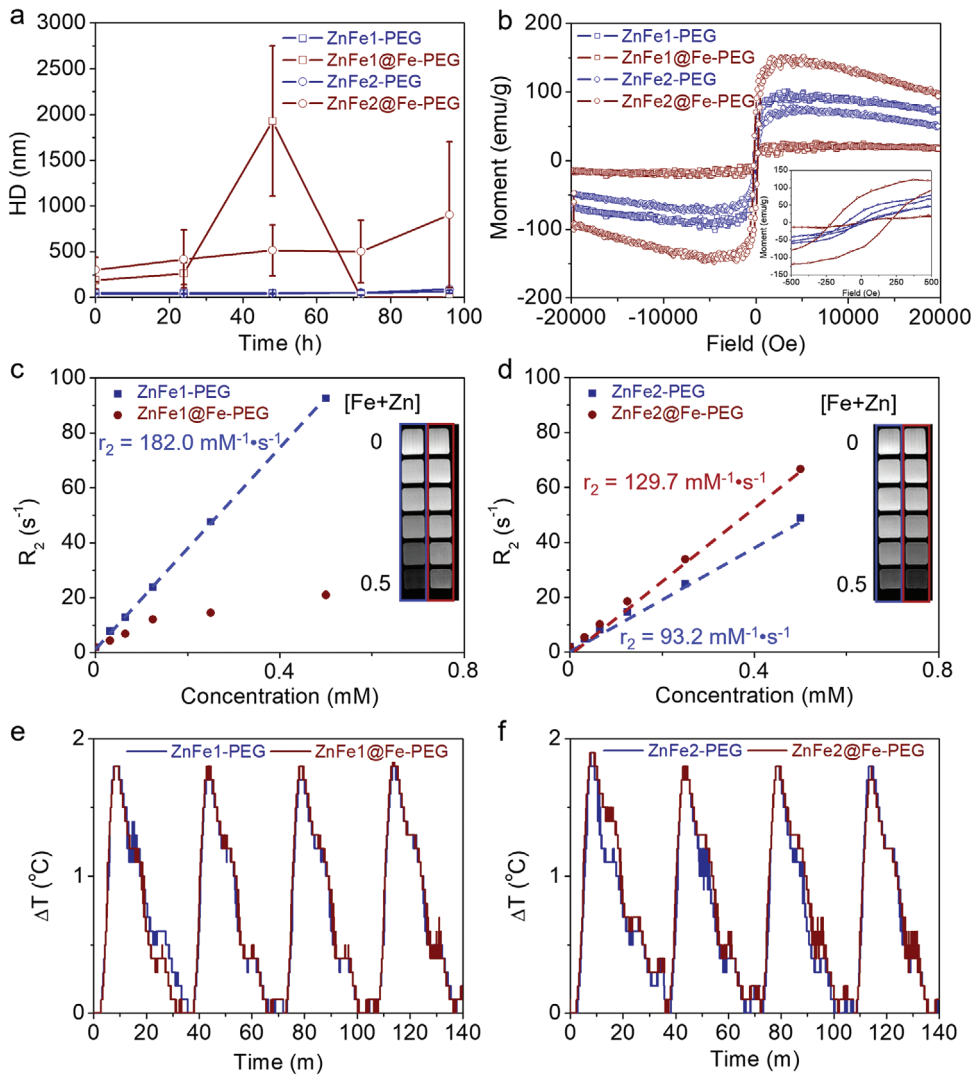

Figure 2. a) Hydrodynamic diameter (HD) of the synthesized NPs determined in saline at different times using dynamic light scattering (DLS). b) Magnetization versus applied magnetic field (MvsH) measurements of the NPs at 300 K. c,d) Plot of relaxation rate ($1/T_2$) versus the concentration of Fe calculated at 9.4 T, and the linear fits (when it is possible) whose slopes correspond to the transverse relaxivities (r_2). The inset shows the corresponding T_2-weighted images. e,f) Thermal stability test measured under AMF (145.2 kHz and 580 Gauss). Single-core ZnFe-PEG NPs are represented in blue, whereas alloy ZnFe@Fe-PEG NPs are represented in red. The different synthetic routes 1 and 2 are represented with squares and circles, respectively.

that there remain unresolved aspects pertaining magnetism at the nanoscale.

Concerning magnetic relaxivity, the transverse relaxivities (r_2) of ZnFe1-PEG, ZnFe2-PEG, and ZnFe2@Fe-PEG were 182.0, 93.2, and 129.7 mM s^{-1} (Figure 2c,d), respectively. As for ZnFe1@Fe-PEG, it was not possible to measure r_2 due to the extremely high aggregation rate occurring under an external magnetic field. It is also worth noting that the r_2 values of the single-core NPs were comparable to IONPs of ≈20 nm reported by us.[64] In this sense, T_2 values can be mathematically described according to the quantum mechanical outer-sphere theory as:[65]

$$\frac{1}{T_2} = \frac{256\pi^2\gamma^2}{405} V^* M_s^2 \frac{a^2}{D\left(1+\frac{L}{a}\right)} \quad (1)$$

where γ is the proton gyromagnetic ratio, M_S is the saturation magnetization, α is the NP core radius, D is the diffusivity of water molecules, L is the thickness of the organic coating layer of NPs (which can be inferred from the HDs), and V^* is the volume fraction, mathematically described as:

$$V^* = \frac{4\pi a^3}{3000} N_0 M \quad (2)$$

where N_0 is Avogadro's constant, and M is the molarity of NPs suspension.

Since π, γ, D, N_0, and M are constants and, taking into account the TEM diameter, Ms, and HD of our ZnFe NPs, the quantum mechanical outer-sphere theory was not enough to fully explain the obtained r_2 (ZnFe2@Fe-PEG should have lower r_2 compared to ZnFe2-PEG).

Additionally, the magnetic-to-heat conversion of ZnFe NPs was evaluated by their thermal response performance under AMF and the subsequent SAR calculation. The thermal stability was evaluated by measuring the temperature increase in four AMF on-off cycles, resulting in very high stability for all ZnFe NPs (Figure 2e,f). The calculated SAR values were 1730.5, 1454.2, 1510.2, and 1849.8 W g^{-1} for ZnFe1-PEG, ZnFe2-PEG, ZnFe1@Fe-PEG, and ZnFe2@Fe-PEG, respectively. Surprisingly, these SAR values were one order of magnitude higher compared to those of IONPs in the range 20–30 nm, even though the latter were measured under a twofold higher frequency.[66,67] Moreover, the linear response theory model predicts that magnetic NPs of ≈20 nm are optimal in terms of magnetic-to-heat conversion efficiency,[68] which is not fully in agreement with our results since ZnFe1-PEG (≈30 nm) displayed greater SAR than ZnFe2-PEG (≈20 nm), but lower than ZnFe2@Fe-PEG (≈22 nm).

Concerning the mathematical analysis of the SAR, although some controversy exists, there are mainly three different components described as: 1) hysteresis loss, 2) relaxation losses (Brownian relaxation (τ_B) and Néel relaxation (τ_N)), and 3) eddy current loss.[14] On the one hand, hysteresis loss can be calculated by:[69,70]

$$\text{hysteresis loss} = \frac{f}{m_{NP}} A \tag{3}$$

where A is the area enclosed by the loops, f is the number of loops per second, and m_{NP} is sample concentration (mass per unit volume of the colloidal sample). Both hysteresis loss and eddy current loss are negligible for superparamagnetic NPs. On the other hand, relaxation losses (or effective relaxation time) can be mathematically described as:[71]

$$\tau = \frac{\tau_N \tau_B}{\tau_N + \tau_B} \tag{4}$$

where τ_B and τ_N can be described as:

$$\tau_B = \frac{3\eta V_h}{k_B T} \tag{5}$$

$$\tau_N = \tau_0 e^{KV/k_B T} \tag{6}$$

where η is the dynamic viscosity of carrier liquid, r_h the hydrodynamic radius of the particle, k_B the Boltzmann constant, T the absolute temperature of the system in kelvin, τ_0 is usually in the order of 10^{-9}, K is the anisotropy constant, and V is the particle volume. In this scenario, being ZnFe2@Fe-PEG the only ferromagnetic NPs and possessing the larger HDs, it was expected they had significantly higher SAR. However, although the SAR values of these NPs were actually higher, the differences in SAR with respect to NPs were lower than expected, suggesting that K, which was not evaluated in this work, could play a critical role in the SAR (magnetic-to-heat conversion) of magnetic NPs, as previously pointed out.[13,72,73]

Consequently, our findings imply the need for substantial work in the field of nanomagnetism to gain deeper insight into this phenomenon and elucidate the mechanisms underlying observations such as those presented in this work.

3.2. In Vitro Cytotoxicity Assessment

HFF-1 cells were selected as the working model and exposed to increasing concentrations of NPs from 0.1 to 100 μg mL^{-1} (Fe+Zn). Both ZnFe1-PEG and ZnFe2-PEG did not induce appreciable changes in HFF-1 cell morphology (**Figure 3a**). In addition, these single-core NPs did not produce significant changes in either the total number of cells, the intracellular esterase activity, the mitochondrial activity, or dead cells percentage (Figure 3b–e). In the case of alloy ZnFe@Fe-PEG NPs, harmony software could not evaluate the healthy cells above a concentration of 10 μg mL^{-1} because of their aggregation and sedimentation. However, a similar nucleus pattern (blue fluorescence) to single-core ZnFe-PEG NPs was qualitatively observed, together with a mitochondrial activity of HFF-1 cells ≥90% for both ZnFe1@Fe-PEG and ZnFe2@Fe-PEG. All these results evidenced the low cytotoxicity of these alloy ZnFe@Fe-PEG NPs.

Table 1 summarizes the results described so far in this work. Since stability and cytotoxicity are the crucial points that must be fully fulfilled for biomedical applications, both ZnFe1@Fe-PEG and ZnFe2@Fe-PEG were discarded for further experiments due to their poor stability. On the contrary, both ZnFe1-PEG and ZnFe2-PEG exhibited high stability and negligible cytotoxicity, with ZnFe1-PEG having higher r_2 and SAR. Therefore, ZnFe1-PEG NPs were selected as the most promising candidate for in vivo experiments.

3.3. Studies in Non-Tumor-Bearing Mice

The selected ZnFe1-PEG NPs were assessed for their potential as MH mediators for tumor therapy following intravenous administration. Firstly, dynamic T_2-weighted MRI was used to evaluate their short-term (30 min) in vivo pharmacokinetics in different organs, especially in the liver and spleen, due to their prevalent role in NPs excretion pathways.[74,75] Interestingly, these organs displayed two different behaviors (**Figure 4a,b**), with the liver reaching the maximum signal increase a few seconds after NPs injection (≈40%), which remained stable until the end of the experiment, while the spleen signal underwent a slow and continuous increase up to ≈30% at the end of the experiment. These different pharmacokinetics are attributable to differences in the endocytic/phagocytic affinity between Kupffer cells and splenic macrophages for NPs.[76] As expected, no signal changes were observed in any case for muscle, which was used as control tissue. Additionally, long-term pharmacokinetics were evaluated up to 24 h by quantitative T_2 mapping (Figure 4c), along with high-resolution respiration-gated T_2-weighted images for better visualization. A clear darkening was observed both in the liver and spleen 1 h after the injection of ZnFe1-PEG, being more pronounced at 24 h in the liver and, partially recovering toward basal values in the spleen, likewise evidencing the different interaction of NPs with these tissues, as previously mentioned. Moreover, the quantitative evaluation denoted a considerable R_2 increase (or T_2 decay) at 1 h, with ΔR_2 of ≈7.8 and ≈11 s^{-1}, for the liver and spleen, respectively. At 24 h, ΔR_2 was ≈11.5 and ≈8 s^{-1} for liver and spleen, respectively (Figure 4d). Furthermore, the IONPs clearance was expected to be between 48 and 168 h, as previously described by some of us.[77,78]

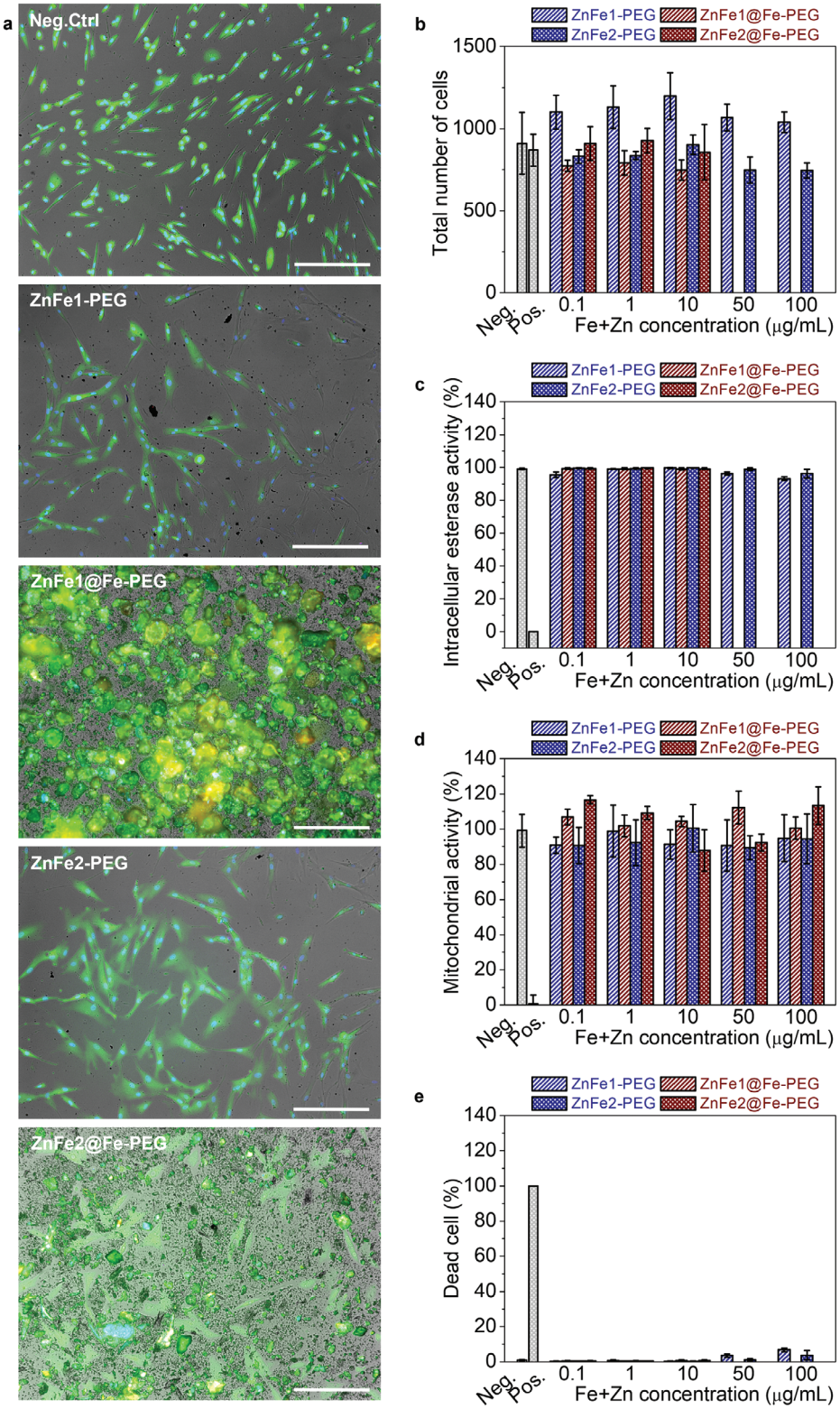

Figure 3. a) Representative optical microscopy images of HFF-1 fibroblasts without exposition (Neg. Ctrl) and after exposure to 100 μg mL^{-1} (Fe+Zn concentration) of single ZnFe and alloy ZnFe@Fe NPs ($n = 5$). These images result from the merge of brightfield (gray), DAPI (blue), TO-PRO-3 iodide (red), and Calcein AM (green). The scale bar corresponds to 50 μm. b) Total number of cells per well, c) intracellular esterase activity (%), d) mitochondrial activity (%), and e) dead cells (%) of HFF-1 fibroblasts after exposure to increasing concentrations (0.1–100 μg mL^{-1} of Fe) of single-core ZnFe and alloy ZnFe@Fe NPs, respectively. Single-core ZnFe NPs are represented in blue, whereas alloy ZnFe@Fe NPs are represented in red. Both negative and positive controls are represented in gray.

Table 1. Summary of the different evaluated parameters.

NPs	Fe [%]	Zn [%]	HD [nm]	Ms [emu g^{-1}]	r_2 [мм$^{-1}$ s^{-1}]	SAR [W g^{-1}]	Thermal stability	Cytotoxicity
ZnFe1-PEG	≈63	≈37	≈50	92.5	182	1730.5	High	Negligible
ZnFe1@Fe-PEG	≈90	≈10	Not stable	21.5	N.A.	1510.2	High	Negligible
ZnFe2-PEG	≈58	≈42	≈60	68.2	93.2	1454.2	High	Negligible
ZnFe2@Fe-PEG	≈99	≈1	≈900	134.9	129.7	1849.8	High	Negligible

The potential in vivo toxicity of ZnFe1-PEG was addressed by the histological analysis of tissue sections of the main organs stained with H&E (**Figure 5a**). Normal tissue architecture was observed in all analyzed organs (liver, kidney, spleen, and lung) without any sign of tissue damage, such as necrosis or infiltrations of inflammatory cells.[79] Therefore, these results confirmed the high biocompatibility of ZnFe1-PEG. Moreover, liver sections were stained with Prussian blue (PB) in order to determine the distribution of ZnFe1-PEG NPs, showing their predominant location inside Kupffer cells, with negligible uptake by hepatocytes (Figure 5b). These results proved that hepatobiliary elimination is the predominant clearance pathway for ZnFe1-PEG. Regarding the PB staining of spleen sections, it must be borne in mind that this tissue removes unhealthy, old, and misshapen red blood cells from the bloodstream, which results in blue staining even in the control tissues.

3.4. Studies in a Breast Cancer Model

Firstly, the efficiency of the EPR effect was evaluated in the 4T1 breast cancer model. No changes were observed in the tumor

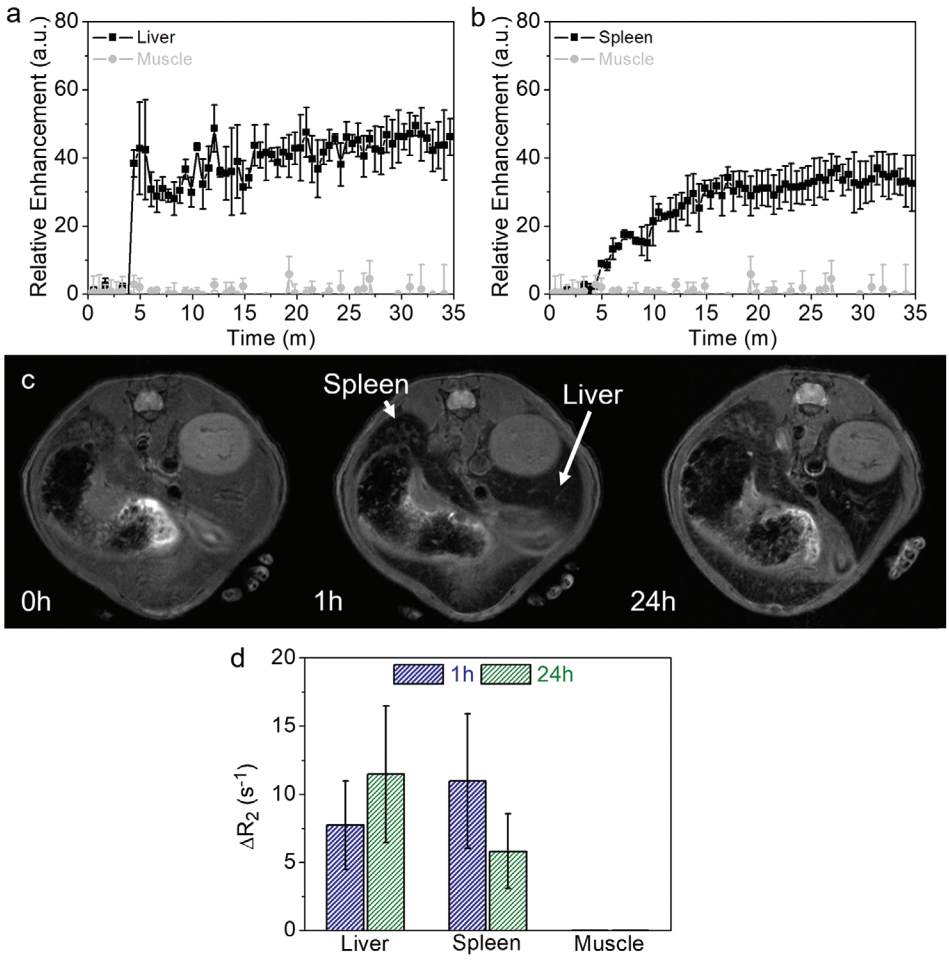

Figure 4. In vivo time courses of a) liver and b) spleen of mice after the intravenous injection of ZnFe1-PEG NPs (10 mg Fe per animal kg). Muscle was used as control tissue (gray in both cases). c) Representative T_2-weighted MR images at different experimental time points after the intravenous injection of ZnFe1-PEG. d) ΔR_2 values of different organs at 1 and 24 h after the intravenous injection of ZnFe1-PEG NPs. The average values were obtained by performing four experiments.

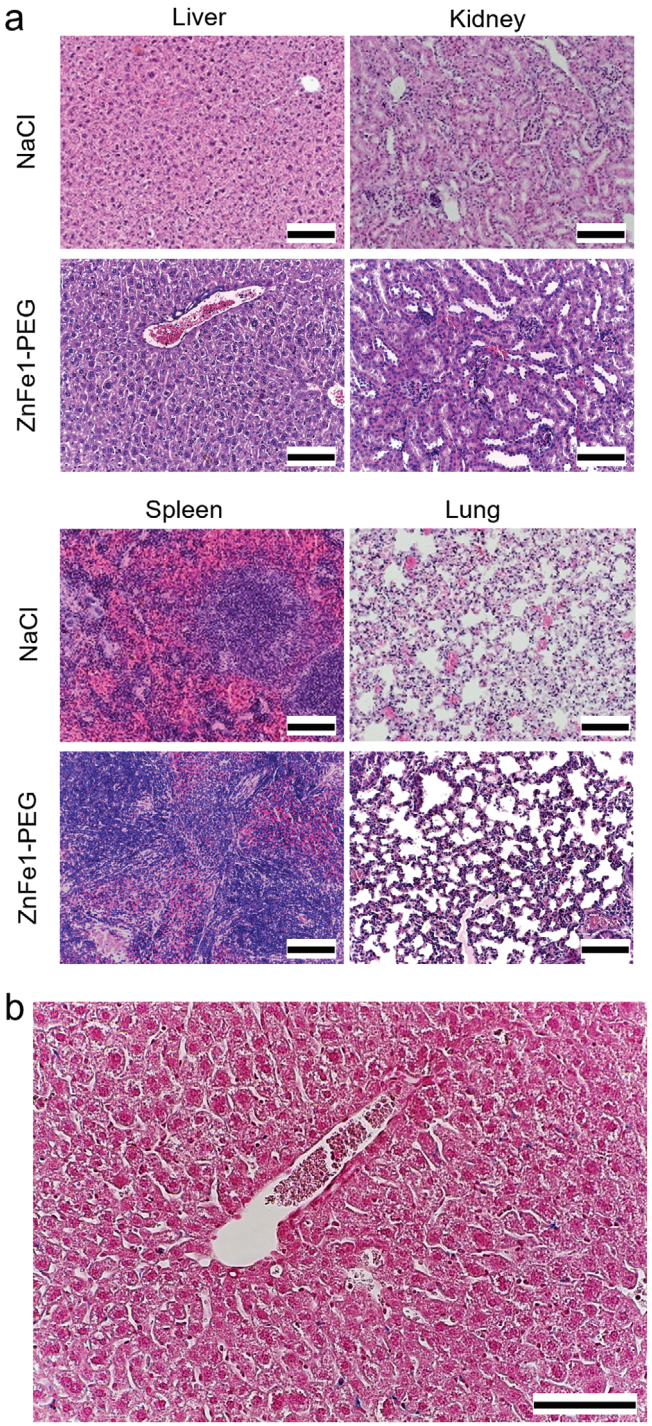

Figure 5. a) Representative histological sections of the main organs: liver, kidney, spleen, and lung of mice at 24 h after the intravenous administration of saline (top) and ZnFe1-PEG NPs (bottom). The scale bar corresponds to 100 µm. b) Representative histological sections of PB staining of the liver at 24 h post-injection of ZnFe1-PEG. The scale bar corresponds to 100 µm.

either by dynamic MRI over the first 35 min or in the T_2-weighted images at 1 h post intravenous injection of ZnFe1-PEG (data not shown). On the contrary, T_2-weighted images at 24 h revealed a noticeable darkening in the tumor periphery, with a darker ring on a deeper zone and no changes in the tumor core, likely due to its characteristic avascular necrotic nature (**Figure 6**a). These results were in agreement with previous studies reporting 24 h as the optimum time frame for an efficient EPR effect.[80–82]

The quantitative analysis showed a slight T_2 decay ($\Delta R_2 \approx 2.5\ s^{-1}$) for the whole tumor, being substantially higher ($\Delta R_2 \approx 5\ s^{-1}$) ($p < 0.05$) in the zone of higher NPs accumulation (Figure 6b). Since the ability of any compound to reach and accumulate in the tumor tissue strongly depends on its vascular permeability, it was evaluated at the end of each experiment (24 h after the administration of ZnFe1-PEG) by T_1 Dynamic Contrast-Enhanced MRI (DCE-MRI) using a commercial Gd chelate (Gadovist). Our results denoted that 4T1-derived tumors display high vascular permeability at the tumor periphery, characterized by fast and remarkable signal enhancement, whereas minimal signal enhancement was observed in the tumor core, consistent with the presence of avascular necrotic tissue (Figure 6c,d). Interestingly, the highest NPs accumulation occurred in a zone with low vascular permeability, suggesting that once the NPs crossed the tumor vascular endothelium, they diffused to poorly vascularized areas, where they remained trapped due to inefficient drainage mechanisms (absence of blood and lymphatic vessels).

Once an appreciable EPR effect in breast tumors was confirmed, an in vivo therapeutic approach was conducted as a proof-of-concept study to demonstrate the remarkable potential of our NPs as magnetic hyperthermia mediators. While intratumoral administration can be useful in certain cases, it presents some important limitations, primarily associated with the delivery of NPs to non-proliferative regions of the tumor (necrotic zone), which can drastically hamper their therapeutic effectiveness, or with the inaccessible location of the tumor, making the administration of NPs impossible.[38] Therefore, in this work, we investigated the therapeutic efficacy of our NPs when administered intravenously, aiming to effectively target the vascularized/viable parts of the tumors. Two experimental conditions were selected: 1) NaCl+ AMF exposure (MH)+ and 2) intravenous injection of ZnFe1-PEG NPs+ AMF exposure (MH)+. Of note, regarding the AMF parameters, f was selected as the closer allowed by our equipment to the clinical one, while H was selected as the highest allowed one. Volumetric tumor analysis by MRI was used to monitor treatment response. Tumor volume increased over time in both NaCl+ MH+ and ZnFe1-PEG+ MH+, but a considerable delay was observed for the last one, reaching a statistically significant difference ($p < 0.05$) 13 days after a single AMF exposure (**Figure 7**). Moreover, mice of the group NaCl+ MH+ reached animal slaughtering criteria 12 days after the treatment, while animals injected with ZnFe1-PEG NPs reached this stage 7 days later. Although a 7-day difference in lifespan may not appear substantial, it becomes significant when considering the rapid exponential growth of these tumor models. Additionally, to rule out a possible effect of the AMF themselves on tumor growth, the tumor growth curve of group G1 was compared with the standard growth curve of this tumor model determined in our lab under our basal experimental condition, wherein mice were only

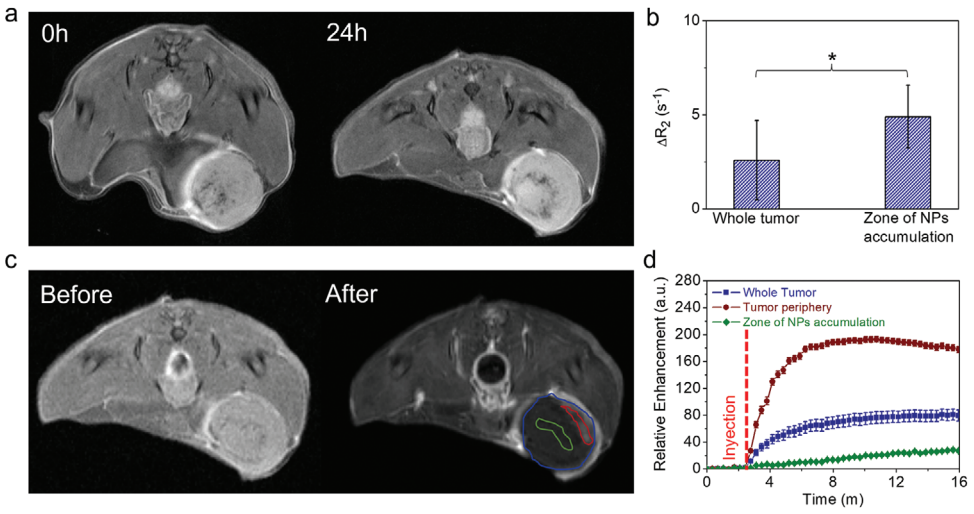

Figure 6. a) Representative T_2-weighted MR images before and 24 h after the intravenous injection of ZnFe1-PEG NPs in 4T1 tumor-bearing mice. b) ΔR_2 values of the whole tumor and the zone of NPs accumulation at 24 h post-administration of ZnFe1-PEG. c) Representative T_1 MR images before and after the intravenous administration of Gadovist. d) In vivo time courses of Gadovist in 4T1 tumor-bearing mice. The average values were obtained by performing four experiments.

administered a NaCl injection. This comparison confirmed that AMF exposure in the absence of NPs does not produce any noticeable effect on tumor growth (see Figure S4, Supporting Information).

It is worth mentioning that, to our knowledge, only a few papers described a successful magnetic hyperthermia treatment after intravenous administration. Huang et al. used a frequency of 980 kHz (far away from the clinical one), an extremely high NPs concentration (1.7 g Fe kg^{-1}), no statistical analysis of the treatment was performed, and the methodology for the tumor volume measurements was not described.[83] Similarly, Albarqi et al. applied a frequency of 420 kHz (not suitable for clinical applications), an even greater NPs concentration (10 g Fe kg^{-1}), four treatment cycles were necessary to achieve statistically significant

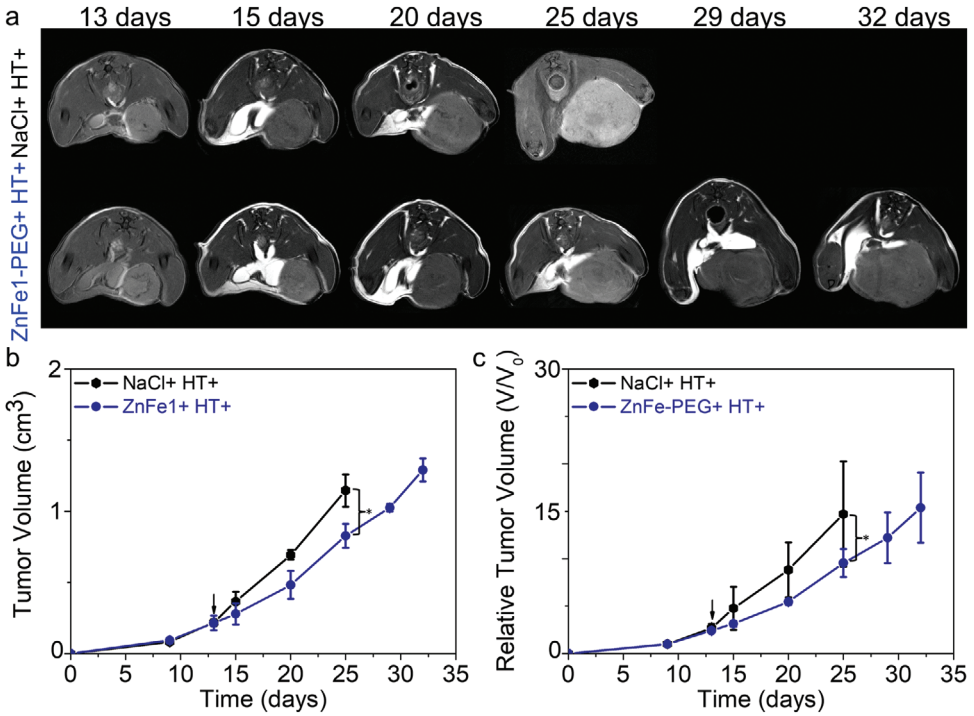

Figure 7. a) Representative T_2-weighted MR images at different experimental times post-tumor implantation. Magnetic hyperthermia treatment was conducted on day 13 ($n = 4$). b) Tumor volume evaluation based on MR images. c) Relative tumor volume evolution evaluation based on MR images. Arrows indicate the treatment day. The statistical test was significant for data with * ($p < 0.05$).

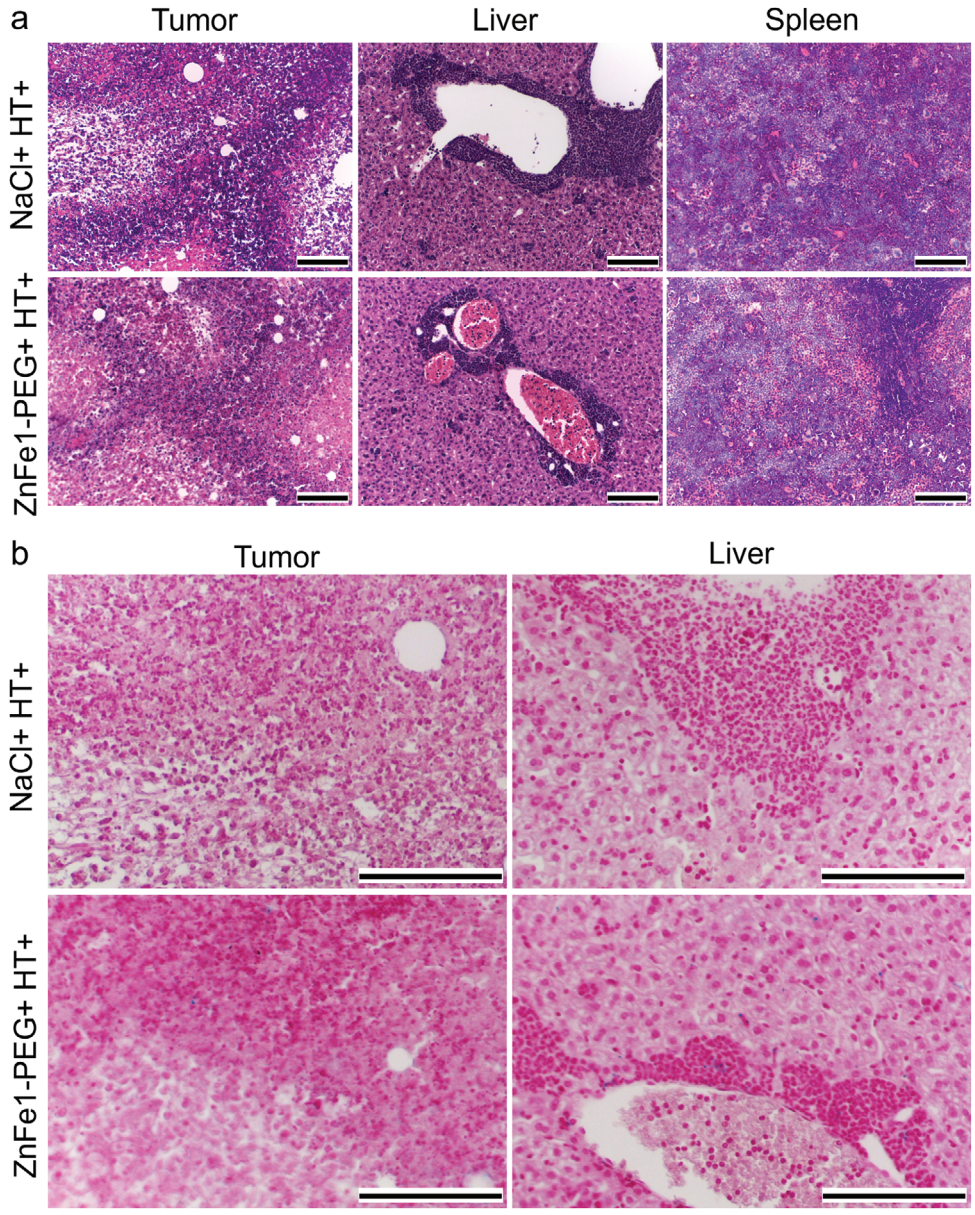

Figure 8. a) Representative histological sections of H&E staining of tumor, liver, and spleen and b) Representative histological sections of PB staining of tumor and liver of 4T1 tumor-bearing mice at the end point of the in vivo therapeutic approach after the administration of NaCl or ZnFe1-PEG and the hyperthermia treatment. The scale bar corresponds to 100 µm.

differences at 28 days after the treatment, and the measurements of tumor volume were done with a caliper, which lacks accuracy and can lead to overestimation of tumor reduction, that is, underestimation of total tumor volume.[84] Soleymani et al. employed a frequency of 150 kHz, animals received four times a moderately high NPs concentration (50 mg Fe kg^{-1}), four treatment cycles were necessary to achieve statistically significant differences 5 days after the treatment, and again, the tumor volume was evaluated with a caliper.[85] Finally, Hu et al. described the encapsulation of hydrophobic 5 nm IONPs within polymeric NPs, alongside chemotherapeutic agents, and conjugated them with IVO24 peptide for active tumor targeting instead of relying on the EPR effect.[86] The authors claim that this platform could be used for controlled drug delivery, magnetic hyperthermia, and MR imaging. However, the SAR values of the system were not provided, nor was MRI carried out, thus precluding the assessment of the actual potential of these NPs as MH mediators or for in vivo MRI-tracking. Also, the tumor size was determined using a caliper, which entails some limitations as already mentioned. Additionally, Herrero de la Parte et al. recently demonstrated in preclinical models that the Hx*f* product (in 10^9 A ms^{-1} units) of the AMF must satisfy a specific combination, limiting the result to ≤9.46 (as per the Atkinson–Brezovich criteria).[87] Given that our Hx*f* product has been calculated to be 2.13×10^9 A ms^{-1}, it can be concluded that our therapeutic approach is entirely deemed safe. Therefore, to the best of our knowledge, we demonstrate, for the

first time, the successful application of intravenously administered MNPs for MRI-tracked MH tumor therapy in passively targeted tumor xenografts using a single NPs low dose and only one AMF exposure at frequencies suitable for clinical application.

Histological analysis was conducted at the end of the experiments to assess tumor tissue status after MH treatment with ZnFe1-PEG NPs. H&E staining was used to assess tissue architecture, and PB staining to ascertain IONPs localization, as mentioned previously. Tumor sections exhibited the characteristic high cell density commonly found in solid tumors and a heterogeneous cytoarchitecture (**Figure 8a**). Furthermore, metastatic tumor granulocytes were clearly observed in the liver, as expected for this well-known metastatic tumor model, and in line with previous studies by some of us.[88] It should be noted that even 7 days later, from a qualitative point of view, tumor sections from mice injected with of ZnFe1-PEG NPs presented a lower number of cell nuclei (in purple), besides a smaller metastatic area in the liver, compared to NaCl+ MH+ mice. Concerning the spleen, an increase of up to tenfold normal weight was noticed, as well as an expanded red pulp with a significant reduction in the white pulp area. These hallmarks are indicative of splenomegaly derived from tumor growth factors in 4T1 tumor-bearing mice, as previously pointed out.[89] Furthermore, PB staining of tumor and liver tissue still denoted blue spots in both primary tumor and metastatic lesions, even 7 days after ZnFe1-PEG NPs administration, but not in either hepatocytes or Kupffer cells evidencing the completely hepatobiliary excretion at this time point. These remanent NPs could potentially be used for subsequent AMF expositions, although further experiments are required to determine the optimum number of AMF expositions. Of note, no evidence of blue staining was observed in Kupffer cells, which could be assumed as a total hepatobiliary excretion of ZnFe1-PEG NPs in one week.

4. Conclusion

In this work, we performed the synthesis of three single-core (ZnFe1, ZnFe2, and ZnFe3) NPs, with one of them, ZnFe3, being discarded because of its heterogeneity. Then, based on classical LaMer theory, we attempted the synthesis of core–shell structures using these single-core NPs as seeds. Rather than that, an unexpected metallic reorganization was observed. These results demonstrate that classical theories on nucleation and growth are not able to fully predict the final size/shape of NPs, pointing out the imperative need for further research in the field of nanomagnetism.

On the other hand, our results showed that both single-core and alloy NPs presented enhanced magnetic features as MRI CAs and, most importantly, as magnetic-to-heat conversion mediators, with a remarkably higher SAR, as compared to IONPs in a similar size range. Furthermore, unlike most MNPs developed for MH purposes, ZnFeNP1-PEG was capable of passively accumulating within tumors via the EPR effect. This effective passive tumor targeting and improved SAR properties enabled effective tumor treatments through intravenous injection, even after a single administration of a low NPs concentration, together with one exposure to an AMF frequency suitable for clinical applications. To our knowledge, this is the first report demonstrating a successful therapeutic response to MH using intravenously administered MNPs at low concentrations and applying only one AMF cycle at clinical frequency. Finally, PB staining showed NPs remaining in the tumor even 19 days after their administration, which could be exploited for multiple AMF exposures or for prolonged drug delivery mediated by NPs.

Supporting Information

Supporting Information is available from the Wiley Online Library or from the author.

Acknowledgements

Financial support was provided by grant P20_00727/PAIDI2020, funded by the Consejería de Transformación Económica, Industria, Conocimiento y Universidades, Junta de Andalucía, Spain; grant no. CTQ2017-86655-R, funded by the Ministerio de Economia, Industria y Competitividad, Spain; and grant no. PID2020-118448RBC21, funded by MCIN/AEI/10.13039/501100011033. C.C. acknowledges the support of his senior postdoctoral grant no. RH-0040-2021, funded by the Consejería de Salud y Familias, Junta de Andalucía. Financial support was also provided through the contract granted to J.D.U.-G., funded by the European Union—NextGenerationEU, and the *Plan de Recuperación, Transformación y Resiliencia*, through grant no. MA/INV/0008/2022 by the Consejería de Empleo, Formación y Trabajo Autónomo of the Junta de Andalucía in the 2022 call of the Programa Investigo, Mecanismo de Recuperación y Resiliencia; and through the contract granted to I.M.-S., funded by the Fondo Social Europeo, Iniciativa de Empleo Juvenil, through grant no. POEJ_00027 by the Consejería de Transformación Económica, Industria, Conocimiento y Universidades of the Junta de Andalucía. The authors thank Juan F. López for assistance with TEM experiments, Maria Isabel Castillo for assistance with animal manipulations, and Maria Somoza and Marta Carayol for assistance with MRI experiments. ICP-MS was conducted at Servicios Centrales de Investigación de la Universidad de Málaga. TEM, optical microscopy, relaxivity measurements, and MRI experiments were performed in the ICTS "NANBIOSIS," more specifically in the U28 Unit at the Instituto de Investigación Biomédica de Málaga y Plataforma en Nanomedicina (IBIMA Plataforma B*IONAND*). The authors also thank to the Research Facilities of Universidad de Sevilla, CITIUS for the use of the STEM microscope.

Conflict of Interest

The authors declare no conflict of interest.

Data Availability Statement

The data that support the findings of this study are available from the corresponding author upon reasonable request.

Keywords

advanced therapies, cancer, classical nucleation and growth theories, contrast agent, MRI, nanomagnetism, zinc ferrite nanoparticles

Received: November 17, 2023
Revised: January 18, 2024
Published online:

[1] A. Akbarzadeh, M. Samiei, S. Davaran, *Nanoscale Res. Lett.* **2012**, *7*, 144.

[2] L. H. Reddy, J. L. Arias, J. Nicolas, P. Couvreur, *Chem. Rev.* **2012**, *112*, 5818.
[3] J. Kudr, Y. Haddad, L. Richtera, Z. Heger, M. Cernak, V. Adam, O. Zitka, *Nanomaterials* **2017**, 243, *7*.
[4] W., S. Arora, *Int. J. Nanomed.* **2012**, *7*, 3445.
[5] M. Mahmoudi, S. Sant, B. Wang, S. Laurent, T. Sen, *Adv. Drug Delivery Rev.* **2011**, *63*, 24.
[6] N. Tran, T. J. Webster, *J. Mater. Chem.* **2010**, *20*, 8760.
[7] J. G. Ku, X. Y. Liu, H. H. Chen, R. D. Deng, Q. X. Yan, *AIP Adv.* **2016**, *6*, 025004.
[8] K. M. Krishnan, *IEEE Trans. Magn.* **2010**, *46*, 2523.
[9] L. Maldonado-Camargo, M. Unni, C. Rinaldi, in *Biomedical Nanotechnology: Methods and Protocols*, Eds.: S. H. Petrosko, E. S. Day, Springer, New York, NY, **2017**, pp. 47–71.
[10] H. Gavilan, S. K. Avugadda, T. Fernandez-Cabada, N. Soni, M. Cassani, B. T. Mai, R. Chantrell, T. Pellegrino, *Chem. Soc. Rev.* **2021**, *50*, 11614.
[11] T. Tatarchuk, M. Bououdina, W. Macyk, O. Shyichuk, N. Paliychuk, I. Yaremiy, B. Al-Najar, M. Pacia, *Nanoscale Res. Lett.* **2017**, *12*, 141.
[12] J. Hwang, M. Choi, H.-S. Shin, B.-K. Ju, M. Chun, *Appl. Sci.* **2020**, *10*, 6279.
[13] J.-H. Lee, J.-t. Jang, J.-s. Choi, S. H. Moon, S.-h. Noh, J.-w. Kim, J.-G. Kim, I.-S. Kim, K. I. Park, J. Cheon, *Nat. Nanotechnol.* **2011**, *6*, 418.
[14] M. R. Phadatare, J. V. Meshram, K. V. Gurav, J. H. Kim, S. H. Pawar, *J. Phys. D: Appl. Phys.* **2016**, *49*, 095004.
[15] V. Nica, C. Caro, J. M. Paez-Munoz, M. P. Leal, M. L. Garcia-Martin, *Nanomaterials* **2020**, *10*, 907.
[16] T. Stylianopoulos, *Ther. Delivery* **2013**, *4*, 421.
[17] A. Avasthi, C. Caro, E. Pozo-Torres, M. P. Leal, M. L. Garcia-Martin, *Top. Curr. Chem.* **2020**, *378*, 40.
[18] C. Caro, A. Avasthi, J. M. Paez-Muñoz, M. Pernia Leal, M. L. García-Martín, *Biomater. Sci.* **2021**, *9*, 7984.
[19] F. Fernandez-Alvarez, C. Caro, G. Garcia-Garcia, M. L. Garcia-Martin, J. L. Arias, *J. Mater. Chem. B* **2021**, *9*, 4963.
[20] Y. Chang, N. Liu, L. Chen, X. Meng, Y. Liu, Y. Li, J. Wang, *J. Mater. Chem.* **2012**, *22*, 9594.
[21] M. Norouzi, V. Yathindranath, J. A. Thliveris, B. M. Kopec, T. J. Siahaan, D. W. Miller, *Sci. Rep.* **2020**, *10*, 11292.
[22] A. J. Giustini, A. A. Petryk, S. M. Cassim, J. A. Tate, I. Baker, P. J. Hoopes, *Nano LIFE* **2010**, *01*, 17.
[23] D. Chang, M. Lim, J. Goos, R. Qiao, Y. Y. Ng, F. M. Mansfeld, M. Jackson, T. P. Davis, M. Kavallaris, *Front. Pharmacol.* **2018**, *9*, 831.
[24] X. Liu, Y. Zhang, Y. Wang, W. Zhu, G. Li, X. Ma, Y. Zhang, S. Chen, S. Tiwari, K. Shi, S. Zhang, H. M. Fan, Y. X. Zhao, X. J. Liang, *Theranostics* **2020**, *10*, 3793.
[25] H. Sung, J. Ferlay, R. L. Siegel, M. Laversanne, I. Soerjomataram, A. Jemal, F. Bray, *Ca-Cancer J. Clin.* **2021**, *71*, 209.
[26] R. Garcia-Figueiras, S. Baleato-Gonzalez, A. R. Padhani, A. Luna-Alcala, J. A. Vallejo-Casas, E. Sala, J. C. Vilanova, D. M. Koh, M. Herranz-Carnero, H. A. Vargas, *Insights Imaging* **2019**, *10*, 28.
[27] M. Haris, S. K. Yadav, A. Rizwan, A. Singh, E. Wang, H. Hariharan, R. Reddy, F. M. Marincola, *J. Transl. Med.* **2015**, *13*, 313.
[28] Z. Zhou, Z. R. Lu, *Wiley Interdiscip. Rev.: Nanomed. Nanobiotechnol.* **2013**, *5*, 1.
[29] E. Lancelot, J. S. Raynaud, P. Desche, *Invest. Radiol.* **2020**, *55*, 578.
[30] M. Scorsetti, P. Navarria, F. Pessina, A. M. Ascolese, G. D'Agostino, S. Tomatis, F. De Rose, E. Villa, G. Maggi, M. Simonelli, E. Clerici, R. Soffietti, A. Santoro, L. Cozzi, L. Bello, *BMC Cancer* **2015**, *15*, 486.
[31] V. Schirrmacher, *Int. J. Oncol.* **2019**, *54*, 407.
[32] D. Egea-Benavente, J. G. Ovejero, M. D. P. Morales, D. F. Barber, *Cancers* **2021**, *13*, 4583.
[33] M. Schwake, M. Müther, A.-K. Bruns, B. Zinnhardt, N. Warneke, M. Holling, S. Schipmann, B. Brokinkel, J. Wölfer, W. Stummer, O. Grauer, *Cancers* **2022**, *14*, 541.
[34] U. Gneveckow, A. Jordan, R. Scholz, V. Brüß, N. Waldöfner, J. Ricke, A. Feussner, B. Hildebrandt, B. Rau, P. Wust, *Med. Phys.* **2004**, *31*, 1444.
[35] F. K. H. van Landeghem, K. Maier-Hauff, A. Jordan, K.-T. Hoffmann, U. Gneveckow, R. Scholz, B. Thiesen, W. Brück, A. von Deimling, *Biomaterials* **2009**, *30*, 52.
[36] C. Caro, D. Pozo, *Curr. Pharm. Des.* **2015**, *21*, 4822.
[37] M. A. Subhan, S. S. K. Yalamarty, N. Filipczak, F. Parveen, V. P. Torchilin, *J. Pers. Med.* **2021**, *11*, 571.
[38] A. Pandey, A. N. Nikam, B. S. Padya, S. Kulkarni, G. Fernandes, A. B. Shreya, M. C. García, C. Caro, J. M. Páez-Muñoz, N. Dhas, M. L. García-Martín, T. Mehta, S. Mutalik, *Coord. Chem. Rev.* **2021**, *435*, 213826.
[39] J. W. Nichols, Y. H. Bae, *J. Controlled Release* **2014**, *190*, 451.
[40] Y. Nakamura, A. Mochida, P. L. Choyke, H. Kobayashi, *Bioconjugate Chem.* **2016**, *27*, 2225.
[41] J. Park, K. An, Y. Hwang, J. G. Park, H. J. Noh, J. Y. Kim, J. H. Park, N. M. Hwang, T. Hyeon, *Nat. Mater.* **2004**, *3*, 891.
[42] M. Pernia Leal, C. Caro, M. L. García-Martín, *Nanoscale* **2017**, *9*, 8176.
[43] E. Pozo-Torres, C. Caro, A. Avasthi, J. M. Páez-Muñoz, M. L. García-Martín, I. Fernández, M. Pernia Leal, *Soft Matter* **2020**, *16*, 3257.
[44] C. Caro, M. Carmen Muñoz-Hernández, M. P. Leal, M. L. García-Martín, in *Preclinical MRI: Methods and Protocols*, Eds.: M. L. García Martín, P. L Larrubia, Springer, New York, NY, **2018**, pp. 409–419.
[45] V. K. LaMer, R. H. Dinegar, *J. Am. Chem. Soc.* **1950**, *72*, 4847.
[46] V. K. L. Mer, *Ind. Eng. Chem.* **1952**, *44*, 1270.
[47] N. T. K. Thanh, N. Maclean, S. Mahiddine, *Chem. Rev.* **2014**, *114*, 7610.
[48] E. C. Vreeland, J. Watt, G. B. Schober, B. G. Hance, M. J. Austin, A. D. Price, B. D. Fellows, T. C. Monson, N. S. Hudak, L. Maldonado-Camargo, A. C. Bohorquez, C. Rinaldi, D. L. Huber, *Chem. Mater.* **2015**, *27*, 6059.
[49] W. Xie, Z. Guo, F. Gao, Q. Gao, D. Wang, B. S. Liaw, Q. Cai, X. Sun, X. Wang, L. Zhao, *Theranostics* **2018**, *8*, 3284.
[50] G. Cotin, C. Kiefer, F. Perton, D. Ihiawakrim, C. Blanco-Andujar, S. Moldovan, C. Lefevre, O. Ersen, B. Pichon, D. Mertz, S. Begin-Colin, *Nanomaterials* **2018**, *8*, 881.
[51] W. R. Lee, M. G. Kim, J. R. Choi, J. I. Park, S. J. Ko, S. J. Oh, J. Cheon, *J. Am. Chem. Soc.* **2005**, *127*, 16090.
[52] J. R. Shimpi, D. S. Sidhaye, B. L. V. Prasad, *Langmuir* **2017**, *33*, 9491.
[53] G. Van Tendeloo, S. Bals, S. Van Aert, J. Verbeeck, D. Van Dyck, *Adv. Mater.* **2012**, *24*, 5655.
[54] C. Arévalo, A. M. Beltrán, I. Montealegre-Meléndez, E. M. Pérez-Soriano, M. Kitzmantel, E. Neubauer, *Mater. Res. Express* **2019**, *6*, 116518.
[55] J. S. Du, K. He, Y. Xu, C. B. Wahl, D. D. Xu, V. P. Dravid, C. A. Mirkin, *Adv. Funct. Mater.* **2021**, *31*, 2105866.
[56] E. Christou, J. R. Pearson, A. M. Beltrán, Y. Fernández-Afonso, L. Gutiérrez, J. M. de la Fuente, F. Gámez, M. L. García-Martín, C. Caro, *Pharmaceutics* **2022**, *14*, 636.
[57] D. P. Nguyen, Q. T. Tran, X. S. Trinh, T. C. Hoang, H. N. Nguyen, H. H. Nguyen, *Adv. Nat. Sci.: Nanosci. Nanotechnol.* **2012**, *3*, 015017.
[58] H. Yang, S. Zhang, R. Cao, X. Deng, Z. Li, X. Xu, *Sci. Rep.* **2017**, *7*, 8686.
[59] U. Kurien, Z. Hu, H. Lee, A. P. Dastoor, P. A. Ariya, *RSC Adv.* **2017**, *7*, 45010.
[60] C. Caro, M. Pourmadadi, M. M. Eshaghi, E. Rahmani, S. Shojaei, A. C. Paiva-Santos, A. Rahdar, R. Behzadmehr, M. L. García-Martín, A. M. Díez-Pascual, *J. Drug Delivery Sci. Technol.* **2022**, *78*, 103938.
[61] L. Li, W. Jiang, K. Luo, H. Song, F. Lan, Y. Wu, Z. Gu, *Theranostics* **2013**, *3*, 595.
[62] W. Wu, Z. Wu, T. Yu, C. Jiang, W. S. Kim, *Sci. Technol. Adv. Mater.* **2015**, *16*, 023501.

[63] C. Pucci, A. Degl'Innocenti, M. Belenli Gumus, G. Ciofani, *Biomater. Sci.* **2022**, *10*, 2103.
[64] C. Caro, D. Egea-Benavente, R. Polvillo, J. L. Royo, M. Pernia Leal, M. L. Garcia-Martin, *Colloids Surf., B* **2019**, *177*, 253.
[65] X. Zhang, B. Blasiak, A. J. Marenco, S. Trudel, B. Tomanek, F. C. J. M. van Veggel, *Chem. Mater.* **2016**, *28*, 3060.
[66] G. Covarrubias, M. E. Lorkowski, H. M. Sims, G. Loutrianakis, A. Rahmy, A. Cha, E. Abenojar, S. Wickramasinghe, T. J. Moon, A. C. S. Samia, E. Karathanasis, *Nanoscale Adv.* **2021**, *3*, 5890.
[67] S. D. Shingte, A. H. Phakatkar, E. McKiernan, K. Nigoghossian, S. Ferguson, R. Shahbazian-Yassar, D. F. Brougham, *Chem. Mater.* **2022**, *34*, 10801.
[68] P. Guardia, R. Di Corato, L. Lartigue, C. Wilhelm, A. Espinosa, M. Garcia-Hernandez, F. Gazeau, L. Manna, T. Pellegrino, *ACS Nano* **2012**, *6*, 3080.
[69] E. A. Périgo, G. Hemery, O. Sandre, D. Ortega, E. Garaio, F. Plazaola, F. J. Teran, *Appl. Phys. Rev.* **2015**, 041302, *2*.
[70] I. Rodrigo, I. Castellanos-Rubio, E. Garaio, O. K. Arriortua, M. Insausti, I. Orue, J. Á. García, F. Plazaola, *Int. J. Hyperthermia* **2020**, *37*, 976.
[71] D. Cabrera, A. Coene, J. Leliaert, E. J. Artés-Ibáñez, L. Dupré, N. D. Telling, F. J. Teran, *ACS Nano* **2018**, *12*, 2741.
[72] G. Cotin, F. Perton, C. Blanco-Andujar, B. Pichon, D. Mertz, S. Bégin-Colin, in *Nanomaterials for Magnetic and Optical Hyperthermia Applications*, Eds.: R. M. Fratila, J. M. De La Fuente, Elsevier, Amsterdam, The Netherlands **2019**, pp. 41–60.
[73] I. Castellanos-Rubio, O. Arriortua, D. Iglesias-Rojas, A. Barón, I. Rodrigo, L. Marcano, J. S. Garitaonandia, I. Orue, M. L. Fdez-Gubieda, M. Insausti, *Chem. Mater.* **2021**, *33*, 8693.
[74] Y. N. Zhang, W. Poon, A. J. Tavares, I. D. McGilvray, W. C. W. Chan, *J. Controlled Release* **2016**, *240*, 332.
[75] W. Poon, Y. N. Zhang, B. Ouyang, B. R. Kingston, J. L. Y. Wu, S. Wilhelm, W. C. W. Chan, *ACS Nano* **2019**, *13*, 5785.
[76] K. M. Tsoi, S. A. MacParland, X.-Z. Ma, V. N. Spetzler, J. Echeverri, B. Ouyang, S. M. Fadel, E. A. Sykes, N. Goldaracena, J. M. Kaths, J. B. Conneely, B. A. Alman, M. Selzner, M. A. Ostrowski, O. A. Adeyi, A. Zilman, I. D. McGilvray, W. C. W. Chan, *Nat. Mater.* **2016**, *15*, 1212.
[77] M. Pernia Leal, S. Rivera-Fernandez, J. M. Franco, D. Pozo, J. M. de la Fuente, M. L. Garcia-Martin, *Nanoscale* **2015**, *7*, 2050.
[78] M. P. Leal, C. Muñoz-Hernández, C. C. Berry, M. L. García-Martín, *RSC Adv.* **2015**, *5*, 76883.
[79] K. E. Ibrahim, M. G. Al-Mutary, A. O. Bakhiet, H. A. Khan, *Molecules* **2018**, *23*, 1848.
[80] B. Borresen, A. E. Hansen, F. P. Fliedner, J. R. Henriksen, D. R. Elema, M. Brandt-Larsen, L. K. Kristensen, A. T. Kristensen, T. L. Andresen, A. Kjaer, *Int. J. Nanomed.* **2020**, *15*, 8571.
[81] A. Karageorgis, S. Dufort, L. Sancey, M. Henry, S. Hirsjarvi, C. Passirani, J. P. Benoit, J. Gravier, I. Texier, O. Montigon, M. Benmerad, V. Siroux, E. L. Barbier, J. L. Coll, *Sci. Rep.* **2016**, *6*, 21417.
[82] G. Song, D. B. Darr, C. M. Santos, M. Ross, A. Valdivia, J. L. Jordan, B. R. Midkiff, S. Cohen, N. Nikolaishvili-Feinberg, C. R. Miller, T. K. Tarrant, A. B. Rogers, A. C. Dudley, C. M. Perou, W. C. Zamboni, *Clin. Cancer Res.* **2014**, *20*, 6083.
[83] H. S. Huang, J. F. Hainfeld, *Int. J. Nanomed.* **2013**, *8*, 2521.
[84] H. A. Albarqi, A. A. Demessie, F. Y. Sabei, A. S. Moses, M. N. Hansen, P. Dhagat, O. R. Taratula, O. Taratula, *Pharmaceutics* **2020**, *12*, 1020.
[85] M. Soleymani, S. Khalighfard, S. Khodayari, H. Khodayari, M. R. Kalhori, M. R. Hadjighassem, Z. Shaterabadi, A. M. Alizadeh, *Sci. Rep.* **2020**, *10*, 1695.
[86] S. H. Hu, B. J. Liao, C. S. Chiang, P. J. Chen, I. W. Chen, S. Y. Chen, *Adv. Mater.* **2012**, *24*, 3627.
[87] B. Herrero de la Parte, I. Rodrigo, J. Gutierrez-Basoa, S. Iturrizaga Correcher, C. Mar Medina, J. J. Echevarria-Uraga, J. A. Garcia, F. Plazaola, I. Garcia-Alonso, *Cancers* **2022**, *14*, 3084.
[88] P. Carrillo, M. Bernal, C. Téllez-Quijorna, A. D. Marrero, I. Vidal, L. Castilla, C. Caro, A. Domínguez, M. L. García-Martín, A. R. Quesada, M. A. Medina, B. Martínez-Poveda, *Biomed. Pharmacother.* **2023**, *158*, 114070.
[89] S. A. DuPre, K. W. Hunter Jr., *Exp. Mol. Pathol.* **2007**, *82*, 12.